Research Article

Željko Mladenović and Saša Gocić*

Effect of electron temperature and concentration on production of hydroxyl radical and nitric oxide in atmospheric pressure low-temperature helium plasma jet: Swarm analysis and global model investigation

https://doi.org/10.1515/phys-2024-0055
received April 04, 2024; accepted June 19, 2024

Abstract: This work presents a numerical analysis by zero-dimensional global model of the influence of electron temperature and concentration on production of OH and NO for helium plasma jet propagating in the atmosphere of humid air. The calculations are done for the constant electron temperatures (1–4 eV) and concentrations (10^{10} cm^{-3} to 10^{14} cm^{-3}). The mole fractions of air and water vapor vary from 100 to 10,000 ppm. The presented analysis reveals that at low electron temperature and H_2O contents, the dissociative electron attachment to O_2 dominates over attachment to H_2O in production of OH. At higher amount, H_2O modifies the high-energy tail of electron distribution function and increases rate coefficients for electron impact processes. Dissociative electron attachment to H_2O dominates in the production of OH at 1 eV and remains important at higher energies when processes with $O(^1D)$, $O(^1S)$, $O_2(^1\Delta)$ produce OH. Impact dissociation of H_2O dominates over the dissociative attachment at 3 and 4 eV. NO comes mainly from air effluent in the plasma and O + NO_2 at 100 ppm of H_2O. Above 2 eV, the conversion process between OH and NO dominates in NO production at higher amount of H_2O. Regarding dependencies on electron concentration, at low electron temperatures, electron distribution function is affected only at 10^{14} cm^{-3}. But in the case of higher temperature, electron concentration and water vapor have negligible influence. The best agreement with measured data is obtained for electron concentration 10^{10} cm^{-3} and at temperature of 2 eV for OH and 10^{12} cm^{-3} and 3 eV for NO.

Keywords: plasma modeling, plasma jet, reactive oxygen and nitrogen species, global model

1 Introduction

Atmospheric pressure low-temperature (cold) plasmas (CAPS) in the last few decades have become an innovative and promising tool for application in biomedicine and agriculture, primarily based on reactive oxygen and nitrogen species (RONS), but also because the fact that CAPS is usually far from the equilibrium state, with the electron temperature of a few electron-volts, while the gas temperature does not exceed much the room temperature [1–10]. RONS is effectively produced by discharges in noble gases (He or Ar), which expand in ambient humid air, or in plasmas generated in gas mixtures which contain air with given amount of water vapor [11–13]. The composition and quantity of RONS in such plasmas depend on the diverse physical and technical parameters of the plasma-generating devices as well as on ambient conditions and contact of plasma with other media beyond atmospheric air, above all, solid or liquid phases. Different kinds of applications require specific sources of plasma (free plasma jet, plasma needle, dielectric barrier discharge, *etc.*) operating on favorable conditions (DC, kHz, MHz or pulse voltages, ideal absorbed power, flow rate, the preferred mol fraction of air and/or water vapor) for the reinforced production of required reactive species. The ability of those plasmas to effectively produce RONS are not only determined by working gas composition but also to the great extent by electron concentration and temperature (mean energy). The rate coefficients of relevant production processes (production rates) are uniquely related to electron energy distribution function (EEDF) and set of cross-section data, as well as of power absorbed from

*** Corresponding author: Saša Gocić,** Department of Physics, Faculty of Sciences and Mathematics, University of Niš, Višegradska 33, 18000, Niš, Serbia, e-mail: sasa.gocic@pmf.edu.rs
Željko Mladenović: Department of Physics, Faculty of Sciences and Mathematics, University of Niš, Višegradska 33, 18000, Niš, Serbia

external voltage supply. A very complex mutual relation exists among all those parameters, and it is obvious that a comprehensive analysis of numerous factors is necessary to clearly establish the most preferred condition for the RONS production. The brief review of variety of experimental data for the electron temperature T_e and electron density n_e in the literature follows. For the helium atmospheric pressure plasma jet (APPJ) driven by high voltage sinusoidal wave with 8.9 kV in magnitude and frequency of 17 kHz, with the assumption of the Maxwellian electron energy distribution function [14], the electron temperature of 1.87 eV is deduced by equating the total volume ionization to the surface particle loss. The electron density value $1.7 \times 10^{11}\,cm^{-3}$ is deduced from the plasma absorbed power, which is assumed equal to the discharge power. The electron density of helium cold atmospheric plasma jet (CAPJ) [15] is measured using the Rayleigh microwave scattering (RMS) method for different values of relative humidity (RH) of air effluent. The authors have reported that an increase in RH from 35% to 80% induces n_e decreasing from $11 \times 10^{11}\,cm^{-3}$ to $4 \times 10^{11}\,cm^{-3}$ at low applied voltage ~ 4.5 kV, and from $4 \times 10^{12}\,cm^{-3}$ to $3.7 \times 10^{12}\,cm^{-3}$ at higher voltage ~7.0 kV. They have related observed behavior of CAPJ to shift of EEDF toward the low-energy region due to extra electron attachment to H_2O molecules. By using the electron density measured in RMS and the results of Boltzmann solver BOLSIG+, the authors calculated the mean electron energy and reported that T_e decreases from 1.8 to 1.1 eV at 4.5 kV, and from 3.3 to 2.4 eV at 7 kV caused by an RH increase from 35 to 80%. At the same time, measured optical emission intensities at 308.9 nm (OH line) and 311.24 nm (NO line) decrease ~26 and ~24% at 4.5 kV, but contrary increase ~20% and ~21% at 7.0 kV, respectively. Measurements of n_e in APPJ by Stark broadening reported by Nikiforov *et al.* [16] give the value up to $10^{16}\,cm^{-3}$ for highly ionized atmospheric pressure (AP) micro-plasma discharges and around $10^{14}\,cm^{-3}$ for low-density, low-temperature discharges suitable for the direct treatment of living tissue.

According to numerical results from our previous paper [17], the electron concentration drops from $4.5 \times 10^{10}\,cm^{-3}$ to $1.0 \times 10^{10}\,cm^{-3}$ for the increasing amount of water vapor in plasma from 100 to 10,000 ppm due to increased electronegativity of the plasma, while the electron temperature, calculated by the energy balance equation, increases from 3 to 4.75 eV necessary to sustain the discharge. Similar results are obtained by the GlobalKIN code for He/H_2O micro-jet by Schröter *et al.* [18]. Also, the electron concentration is more sensitive to changes of air content in plasma, from 100 to 10,000 ppm, and decreases two times at lowest H_2O content and around 20% at highest one. On the other hand, the electron temperature is less sensitive to the content of air and changes below 15% for any content of H_2O.

By fast imaging (ICCD or streak cameras), it was found that the plasma plume, which appeared continuously to the naked eye, was in fact made up of fast-moving plasma structures. So, plasma generated in AP jet is not a continuous medium but rather travels as a train of plasma volumes or pulses of atmospheric pressure streamers/ionization fronts, known as plasma bullets. Some specific features of plasma bullets moving in a thin jet column differ from those of streamers in a free space, as discussed in series of papers [19,20]. These bullets travel through the surrounding air with velocities in the order of 10^4–$10^5\,ms^{-1}$ without the existence of an externally applied electric field in the propagation space. According to this picture, the electron density and electron mean energy in jet have characteristic space distributions. The production mechanism of OH radicals in a pulsed DC plasma jet is studied by a two-dimensional (2D) plasma jet model and a one-dimensional (1D) discharge model in the study by Liu *et al.* [21]. Liu *et al.* [22] present the spatial temporal resolved images characterizing the behavior of bullets propagating in the pure He APPJ, He + 0.5% O_2 APPJ and He + 0.5% N_2 APPJ impinging on water. The differences in bullet propagations are clearly marked by these three mixtures. In the study by Liu *et al.* [23], a positive voltage of 5 kV with the rising time of 1 ns is applied, and the considered air concentrations are 0.001, 0.01, 0.1, 0.5, 1, and 5%. The calculation reveals that the peak position of the electric field moves toward the cathode, and having in mind that the peak position of the electric field is also the position of the propagating bullet, the evaluated bullet velocity is of the order of 10^5 m/s.

One of the most important reactive species among RONS are hydroxyl radical (OH) and nitric oxide (NO), which serve as precursors for other long-lived reactive species such as H_2O_2 or nitric or nitrous acid. The concentrations of OH and NO are measured by LIF measurement technique for similar plasma mixtures as in our recent paper [17], and results are presented in previous studies [24–27]. Brisset *et al.* [28] present measurement and modeling of OH densities in a radiofrequency-driven atmospheric pressure plasma in a plane-parallel geometry, operated in helium with small admixtures of oxygen and water vapor ($He + O_2 + H_2O$). The density of OH is measured under a wide range of conditions by absorption spectroscopy, using an ultrastable laser-driven broad-band light source. These measurements are compared with zero-dimensional (0D) plasma chemical kinetics simulations adapted for high levels of O_2 (1%).

Generally, tailoring the plasma chemistry (*i.e.*, achieving the required composition of RONS) can be done by adjusting

external parameters. But deep understanding of complex plasma chemistry is only possible through numerical modeling or simulation of all relevant processes. With this goal, we used an approach based on zero-dimensional global models. This spatially averaged models are based on solving the particle and energy balance equations locally (at one fixed space point of discharge volume) [29] and thus give the possibility of following very detailed chemical kinetics in complex plasma systems such as CAPS without much of computational burden. The results of global models for various types of helium CAPS and mixtures have been presented in several papers: He/O_2 [30], He/H_2O [31,32], $He/O_2/H_2O$ or He/humid air [17,33–44], and for interaction of plasma with liquid water [45]. In this article, we use the model described in detail in our previous work [17] based on 1,488 reactions and 74 species for the mixture He/humid air, with goal to investigate the effects of electron temperature and concentration as the main plasma parameters on EEDF and production of OH and NO in helium plasma jets, which propagate in atmosphere of the humid air. The calculations were done for a several measured values of T_e and n_e taken from the literature [14–16]. The amount of air in the plasma was taken as 100, 1,000, and 10,000 ppm, while the content of water vapor is varied to be 100, 1,000, 5,000, and 10,000 ppm, taken from the literature [24,25,39,46] as a representative values in the cases when water vapor comes only from humidity of ambient air (first two values) or it is included as a feed gas component. Nonequilibrium EEDF and the rate coefficients for electron impact processes are calculated by numerical solving of Boltzmann equation (BE) using the two-term solver BOLSIG+ [47] with cross-sectional data from Morgan LXCat database [48] and Quantemol-DB [49]. For plasmas with higher electron density (10^{+17} cm^{-3}), an unsteady nonlinear external electric field (NEEF) or the nonlinear external magnetic field (NEMF) was applied for studying gas dynamics attention has been focused on the Bhatnagar-Gross-Krook type of the Boltzmann kinetic equation [50]. An analytical solution of the model equations was given using the moment and the traveling wave methods. The role of the mean velocity, shear stress, viscosity coefficient, and electromagnetic fields is investigated. The authors conclude that NEEF made plasma fluctuate and perturbed strongly compared to the effect of NEMF. So, in the plasma controlling process, we should use the effect of NEMF instead of the effect of NEEF to retain the equilibrium state.

The primary aim of this work is to reveal all important production processes for OH and NO for a very broad range of basic plasma parameters, n_e and T_e, for different tips of helium plasma jets free propagating in humid air. The presented list of references serves to give experimental background for values of those parameters incorporated in our 0D model and BOLSIG+ solver of the Boltzmann kinetic equation. In other words, all values of n_e and T_e in our calculation are taken from real plasma sources, as well as the concentrations of OH and NO used for validation of results of 0D models. So, we do not compare our and their results, but we use them as reliable sources of necessary data. The state-of-the-art numerical models and diagnostic techniques to describe helium jets along with the benchmarking of different experimental measurements in literature and direct comparisons between simulations and measurements are presented in the topical review [51]. The focus is on the most fundamental physical quantities determining discharge dynamics (the electric field, the mean electron energy, and the electron number density). The physics of plasma jets is described for kHz helium plasma jet showing the effect of the different components (tube, electrodes, gas mixing in the plume, target) of the jet system on discharge dynamics.

Section 2 brings details about the global model and input parameters. In Section 3.1, we analyze the influence of electron temperature only on EEDF and rate coefficients for electron impact processes, at the fixed electron concentration of 10^{10} cm^{-3} and different helium/air/water vapor mixtures. Through global modeling, we then analyze differences in chemical kinetics of OH and NO induced by the mean electron energy. Calculation was done for 1, 2, 3, and 4 eV, estimated from the literature. While various models give T_e in the interval 2–4 eV [17,18,52], measured values by spectroscopic methods are 1–1.5 eV, but the authors state that mainly bulk electrons behind the ionization front contribute to the Thomson scattering signal [26]. In Section 3.2, we present the influence of electron concentration only on the main production pathways for OH and NO, through Maxwellianization of EEDF at various mean energies, again for different amounts of air and water vapor in the plasma. Finally, we present all important production and consumption pathways, which determine the chemical kinetics of NO_x and HNO_x species for a wide range of varied discharge parameters in the model. In Section 4, we give the summary of the results and conclusion.

2 Plasma modeling

2.1 Model description

To obtain the better insight into reaction mechanisms for the production and consumption of OH and NO, we use zero-dimensional global model described in detail in our

previous work [17], based on 1,488 reactions and 74 species for the mixture He/humid air. The term "zero-dimensional" model refers to the fact that it calculates chemical composition and analyzes the chemical production and consumption pathways of each plasma species in one fixed point of the discharge. A model is based on numerical solving of the system of coupled particle balance, electron concentration balance, and electron temperature balance equations as follows [12]:

$$\frac{\mathrm{d}n_i}{\mathrm{d}t} = \sum_j \sum_m k_{jm}^{(S)} n_j n_m + \sum_l \sum_p \sum_q k_{lpq}^{(S)} n_l n_p n_q + \frac{F_i^{\mathrm{fgc}}}{V} n_i^{\mathrm{fgc}}(t=0) - n_i \sum_r k_{ir}^{(L)} n_r - n_i \sum_s \sum_f k_{isf}^{(L)} n_s n_f - \frac{F_i}{V} n_i(t), \quad (1)$$

$$\frac{\mathrm{d}}{\mathrm{d}t}(n_{\mathrm{e}} T_{\mathrm{e}}) = \frac{2 S_{\mathrm{abs}}}{3e} - \sum_i k_{\mathrm{eg}}^{\mathrm{el}} n_{\mathrm{e}} n_{\mathrm{gi}} \frac{2 m_{\mathrm{e}}}{M_{\mathrm{gi}}} (T_{\mathrm{e}} - T_{\mathrm{g}}^{\mathrm{e}}) - \frac{2}{3} \sum_j k_{\mathrm{ej}}^{\mathrm{inel}} n_{\mathrm{e}} n_j \varepsilon_{\mathrm{thr}}^{\mathrm{ej}}, \quad (2)$$

where t, n_i, n_j ... n_f denote time and number density of ith, jth ... and fth species, respectively, including electrons. $k_{jm}^{(S)}$ and $k_{ir}^{(L)}$ denote rate coefficients for two-body reactions between jth and mth species and between ith and rth species. Analogously, $k_{lpq}^{(S)}$ and $k_{isf}^{(L)}$ denote rate coefficients for three-body reactions between lth, pth, qth species, and ith, sth, fth species. Superscripts "(S)" and "(L)" stand for ith species "source" and "loss" process, respectively. F_i represents the flow of ith species and superscript "fgc" stands for the "feed gas component," for which an additional source term is included in Eq. (1), which describes the flow from the inlet of the system at starting time of the simulation ($t = 0$). The flow term is not included in Eq. (1), only in the case of electrons. S_{abs} represents the absorbed power from electric field per unit volume of the plasma system (power density). The second and the third terms describe electron energy losses through elastic momentum transfer scattering on heavy particles and through various inelastic scattering processes. $k_{\mathrm{eg}}^{\mathrm{el}}$ and $k_{\mathrm{ej}}^{\mathrm{inel}}$ denote rate coefficients for electron momentum transfer scattering on ith plasma component and specific inelastic scattering on jth component, with concentrations n_{gi} and n_{j}, respectively. $\varepsilon_{\mathrm{thr}}^{\mathrm{ej}}$ denotes energy loss (threshold) for a specific inelastic electron scattering process on the jth plasma component. In the case of superelastic collisions, the third term on the right side of Eq. (2) is used with the "+" sign.

Other calculation methods characteristic for fluid or hybrid models include the analysis of the spatial inhomogeneity of the plasma by solving the system of the fluid equations, and they are related with much more of computational burden. Solving the system of coupled particle balance equations in one fixed point of the plasma allows the insight into chemistry of the very complex chemical composition, which is characteristic for plasmas formed by mixing of He/Ar discharges with open air, with much less computational burden and time. To describe the changes in plasma characteristics and chemical composition along the symmetry axis of the plasma jet, one should use a "plug-flow" approach based on models for the power density, gas temperature, flow velocity, and air fraction obtained by fitting the experimental results, as presented by Van Gaens and Bogaerts [12]. The main goal of this work was not to analyze how the plasma properties change along the axis of the jet but to calculate the concentration of the OH radical and NO at fixed positions and to analyze the influence of electron temperature and concentration inside plasma bullet on production mechanisms for these important precursors for other reactive species.

With the intention of using the various measured values of electron temperature and concentration from the literature [14–16], in this work, we use the global model in the reduced form, and only the equations describing the balance of particle number density for each plasma species are included in calculation. The system of coupled particle balance equations is now expressed as follows:

$$\frac{\mathrm{d}n_i}{\mathrm{d}t} = \sum_R S_{i,R} + \frac{F_i^{\mathrm{fgc}}}{V} n_i^{\mathrm{fgc}}(t=0) - \sum_R L_{i,R} - \frac{F_i}{V} n_i(t), \quad (3)$$

where t and n_i denote time and number density of ith species, respectively. $S_{i,R}$ and $L_{i,R}$ denote the total rates of source (S) and loss (L) of ith species through specific volumetric chemical reactions (R), including two-body and three-body processes. F_i represents the volume (V) averaged flow-in and flow-out term of ith species as in the study by Mladenović and Gocić [17] in units [cm^3/s]. Outlet flow term is included in particle balance equations for all species, while the inlet flow term at starting time of the simulation is included only for feed gas components (fgc). Model includes only gas phase processes due to the lack of data for particle-surface reaction probabilities in atmospheric pressure plasmas, and most of them are measured in low-pressure systems. They are also dependent on experimental conditions such as gas temperature and pressure, mixture, wall material, and surface conditions [53]. In this work, we analyze the production of OH and NO only in the gas phase inside the plasma channel of the jet in which plasma bullets propagate.

We analyze the chemical kinetics of OH and NO for the case of helium jet which propagates in open air, without

any contact with metallic or dielectric surfaces. Also, as stated by Schröter *et al.* [53], an important fact is that probabilities of particle-surface reactions for atmospheric pressure plasmas are rare, most of them measured in low-pressure systems. They are also dependent on experimental conditions such as gas pressure, temperature or mixture, wall material, and surface conditions. Since we analyze the chemical kinetics of OH and NO only in gas phase, and due to the lack of data for probabilities and rates of particle-surface processes for atmospheric pressure plasmas, our global model excludes surface reactions. One should bear in mind that they could be important when modeling some plasma system in contact with metallic or dielectric surfaces.

During simulation, we calculate the percent of contribution for each process in generation and loss for all specific species by dividing the rate of the process $S_{i,R}$ and $L_{i,R}$ with total, summarized rate $\sum_R S_{i,R}$ and $\sum_R L_{i,R}$. According to these statistics, we have extracted the main processes for the production of OH and NO at different conditions depending on electron temperature and electron density at different air and water vapor contents. The values of these parameters are estimated from the literature [14–16,24,25,39,46].

As presented in the studies by Mladenović and Gocić [17], we use BOLSIG+ for the calculation of EEDFs and rate coefficients for electron impact processes separately from the global model. As an effort to realize the coupling between BOLSIG+ and MATLAB calculation, in the first step, we calculate rate coefficients with the mole fractions estimated from the initial gas mixture, for each case of varied air and water vapor contents and run a global model. In the second step, we use the new mole fractions in BOLSIG+ obtained by a global model after 15 ms when our calculation reaches the steady-state conditions and the concentration of the most abundant plasma species, helium, nitrogen, oxygen, and water vapor, with the most pronounced influence on EEDF, remain constant during calculation, same as initial, for each case of varied air and water vapor contents. In numerical solving of BE in BOLSIG+ input cross-sectional data for electron – neutral scattering processes are multiplied by mole fractions for each of the included species [47]. In the next step, we use the new calculated rate coefficients and run the global model to check plasma composition and mole fractions of included species. We have done a few such iterations until reaching the good agreement, meaning that differences in mole fractions obtained by global model and used in BOLSIG+ calculations are at second decimal places or less.

The parameter for calculation of EEDF in BOLSIG+ is the reduced electric field E/N or the corresponding mean electron energy (represented by the electron temperature, although cold atmospheric pressure plasma is not in the equilibrium state). The rate coefficients for electron-neutral scattering processes can be represented as a function of E/N or mean electron energy. We use the second case because one of the important parameters that we vary in this work is electron temperature.

In some cases [14], rate coefficients for electron impact processes are taken in the Arrhenius form with the assumption that electrons have a Maxwell–Boltzmann (MB) distribution at the corresponding temperature. According to our recently presented results [42], when running the global model with rate coefficients obtained from MB EEDF differences of a few orders in magnitude can emerge for concentration of plasma species in comparison to those calculated with rate coefficients obtained from BE EEDF. Differences in EEDF, the most importantly in the high energy tail, strongly affect the rate of high threshold processes such as excitations, dissociations, and ionizations.

The system of Eq. (3) is solved by MATLAB ode15s solver, with relative and absolute tolerances equal to 10^{-10} and 10^{-6}, respectively. A similar calculation procedure was used in our previous works [17,44], In our model, calculations are made with time step of 50 ns up to 15 ms as the final time during which our calculation reaches the steady state. The gas temperature during calculation was 296 K and the flow rate was 5 slm.

3 Results and discussion

In this section, we first calculate the specific nonequilibrium electron energy distribution function by solving the Boltzmann equation $f_{\mathrm{BE}}(\varepsilon)$ for a broad interval of electron temperature and concentration, also varying the amount of air and water vapor in the plasma. All chosen values are taken from the measurements presented in the literature [14–16]. The shape of a specific nonequilibrium EEDF and the most important of its high energy tail is significant for the rate coefficients of the electron impact processes, which are obtained by the numerical integration using the following formula [17]:

$$k_{\mathrm{e}} = \sqrt{2/m_{\mathrm{e}}} \int_{\varepsilon_{\mathrm{thr}}}^{+\infty} \sigma(\varepsilon)\sqrt{\varepsilon} f_{\mathrm{BE}}(\varepsilon)\mathrm{d}\varepsilon, \tag{4}$$

for the specific set of cross section data $\sigma(\varepsilon)$, where m_{e} stands of the electron mass and $\varepsilon_{\mathrm{thr}}$ the energy threshold of the specific scattering processs. As presented in our previous works [17,42], the results of a system of coupled particle balance equations in 0D global model calculation are mostly dependent on the variation of rate coefficients with

electron temperature, reflecting the indirect influence of EEDF and specific cross-sectional data on chemical kinetics of reactive species on fundamental physical basis.

As it is previously mentioned, zero-dimensional global model is spatially homogenized and constructed to study the chemical kinetics of all plasma species locally, in one specific point of a discharge. Thus, it is very unreliable to compare its results with the results of other calculation methods characteristic for fluid (1D or 2D) or hybrid models, which include the analysis of the spatial inhomogeneity. Comparing with the results obtained by global models from the literature [12,18,39,40], we reach the good agreement on higher mean electron energies above 3 eV and electron concentration of 10^{10} cm^{-3}. Our calculation for OH and NO production is made for a free plasma jet that travels in open air without any actual plasma oscillations or waves that can be generated by various effects, for example, the variation of the gas flow rate in time. Results presented in this article give the insight into chemical kinetics of OH and NO in the helium-free jet with the laminar and time constant gas flow. We present the influence of electron temperature and concentration on the kinetics of these important precursors for other reactive species, as the basic plasma parameters that have the specific space distributions in plasma bullets and depend on specific plasma discharge, starting with the calculation of EEDF as the fundamental physical basis.

3.1 Effect of electron temperature on production of OH and NO

Figure 1a and b present BE EEDF calculated for the constant electron concentration 10^{10} cm^{-3} and two values for T_e 1 and 4 eV, respectively. Different amounts of air and water vapor in helium plasma dramatically change the shape of EEDF at 1 eV and its high-energy tail. For 100 ppm of air in mixture, the population of high energy part of EEDF strongly increases with the increase of H_2O amount from 100 to 10,000 ppm. Presented results show that a higher amount of air rises the energy tail of EEDF for the same mean electron energy, requiring higher electric field due to more pronounced electron energy loss in scattering processes. Water vapor has an analogous effect on EEDF, which is more pronounced at lower mean energies as presented in Figure 1a for 1 eV than for 4 eV in Figure 1b.

As a consequence, rate coefficients for the electron impact processes are increased at higher content of air and water vapor, and the effect is more pronounced at lower mean electron energies, as presented in Figure 2 for dissociative electron attachment to H_2O (a), dissociative attachment to O_2 (b), electron impact dissociation of H_2O (c), O_2 (d), N_2 (e), and ionization of O_2 (f). These processes are important for chemical kinetics of reactive species since dissociative attachment to H_2O and O_2 can be regarded as a first step of reaction chain for producing OH (Section 3.1), electron impact dissociation of O_2 and N_2 initially produce O and N as a precursor for the production of OH and NO, respectively, while the ionization processes are important for production of hydrate-cluster ions, which also play a significant role in OH production after few milliseconds when plasma chemistry becomes very complex. In the previous work [17], we have shown that water vapor profoundly increases plasma electronegativity, while in this work, we show that dissociative attachment to H_2O molecules can be also very important for the production of OH radicals at lower mean electron energies.

Figure 3 presents the concentrations of OH calculated by global model at constant electron temperatures 1, 2, 3,

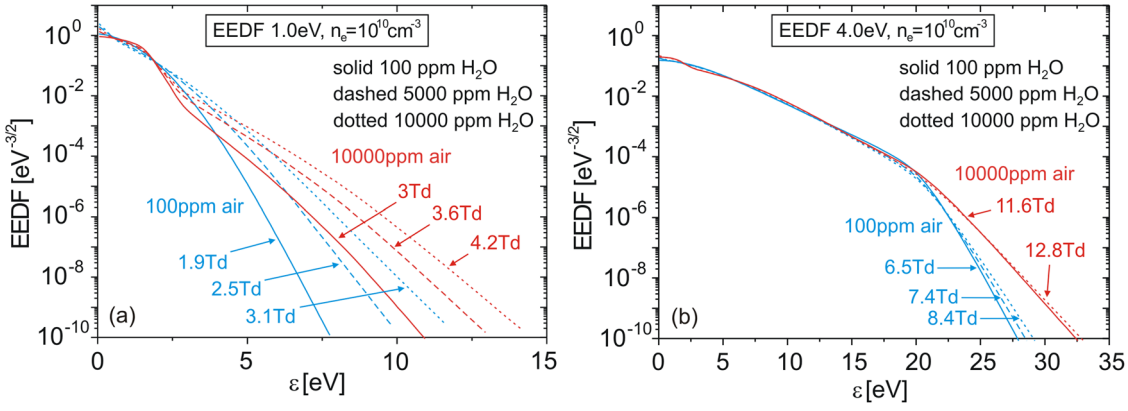

Figure 1: EEDF calculated by BOLSIG+ for (a) mean electron energy 1 eV and (b) 4 eV, for a different amount of air and water vapor in helium plasma and n_e = 10^{10} cm^{-3}.

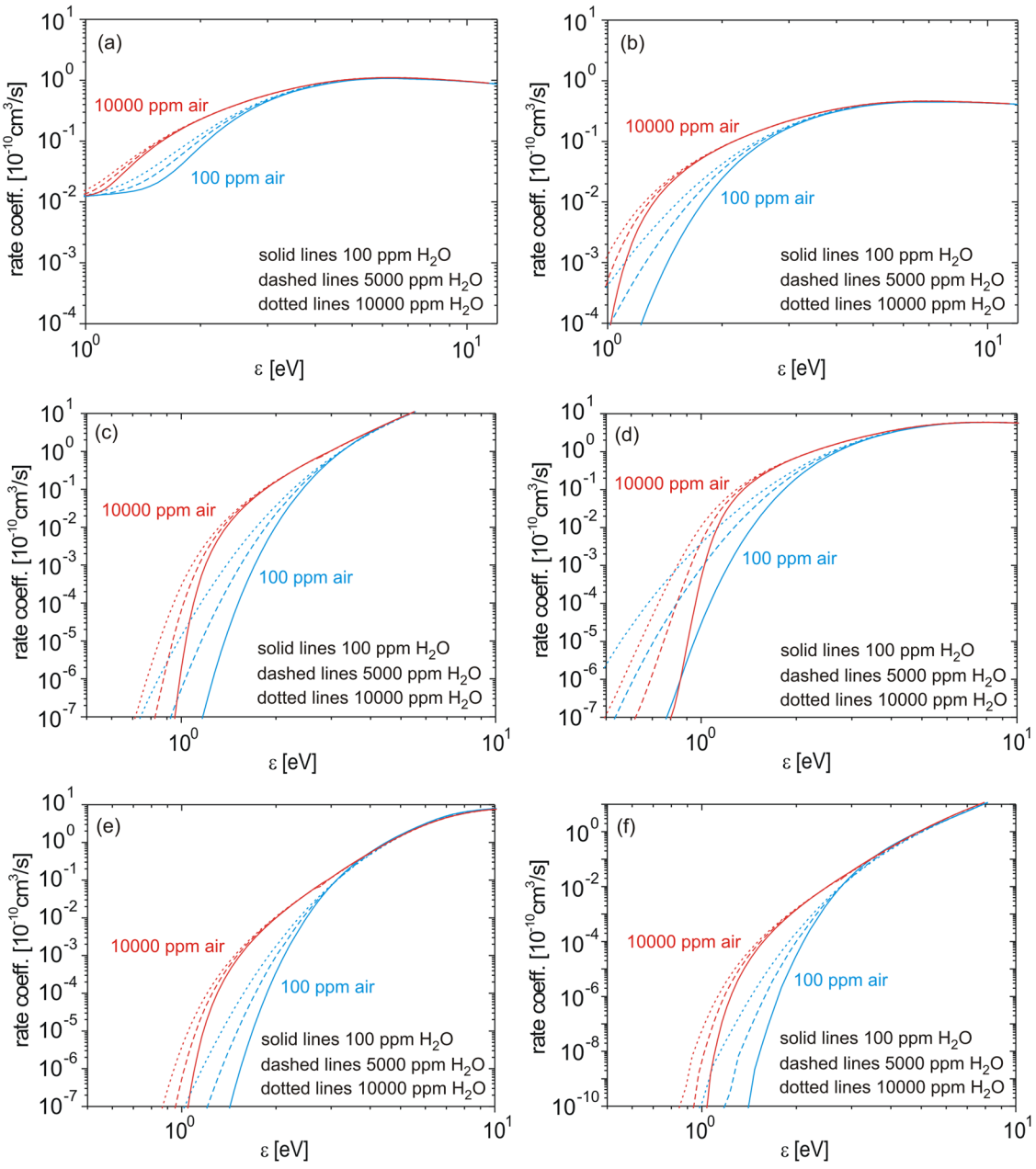

Figure 2: Rate coefficients calculated by BOLSIG+ for (a) electron attachment to H_2O, (b) electron attachment to O_2, (c) dissociation of H_2O, (d) dissociation of O_2, (e) dissociation of N_2 and ionization od O_2, and (f) for a different amount of air and water vapor in helium plasma and $n_e = 10^{10}$ cm^{-3}.

and 4 eV and at different amounts of air and water vapor. The electron concentration is kept constant at 10^{10} cm^{-3} during calculation to analyze the influence of electron temperature on the production of OH. The optimal values of air concentration are chosen from the results of LIF measurement presented in the literature [24] depending on the axial position in the plasma jet. Also, two different concentrations of water vapor are chosen as a representative for the cases when H_2O comes only from the humidity of ambient air (100 ppm of H_2O), or it is included as feed gas component for reinforced production of OH (5,000 ppm of H_2O).

As presented in Figure 3, for a low amount of air in plasma (dashed lines with scatter), the concentration of OH radical is increased with mean electron energy despite the amount of water vapor. At low energies, OH concentrations for 100 and 5,000 ppm of H_2O differ more than for high energies since the rate coefficient for electron impact dissociation of H_2O is not influenced by water vapor above 3 eV (Figure 2b). For higher amount of air (solid lines with

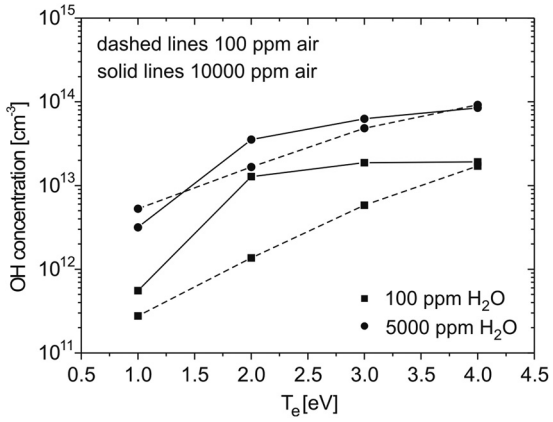

Figure 3: Concentration of OH in plasma as a function of electron temperature for different amounts of air and water vapor in helium plasma and $n_e = 10^{10}$ cm^{-3} after 15 ms.

scatter), chemical kinetics of OH radical is more complex, and there are more important production processes besides electron impact dissociation of H_2O, also depending on mean energy, as presented in Figure 4.

The production of OH radical is initially determined by dissociative electron attachment at 1 eV. In the case of 100 ppm of water vapor, the attachment to O_2 (Figure 4a) is dominant over attachment to H_2O through process $O^- + H_2O \rightarrow OH + OH^-$ and the pathway that includes $H_2O_2^-$ ions produced by the process $O^- + H_2O + He \rightarrow H_2O_2^- + He$. After 15 ms, the composition of the plasma becomes more complex, and chemical reactions of $O_2(^1\Delta)$ and O with HO_2, produced by process $H + O_2 + He \rightarrow HO_2 + He$, become important in the production of OH. At higher mean electron energies and 100 ppm of H_2O, the important pathways are reactions of excited oxygen species $O(^1D)$ and $O(^1S)$ with H_2O molecules due to the increased total rate for electron impact dissociation of O_2. Ion conversion $H_2O^+ + H_2O \rightarrow H_3O^+ + OH$ and process involving hydrate $H_3O^+ \cdot OH$, produced in $O_2^+ \cdot H_2O + H_2O \rightarrow H_3O^+ \cdot OH + O_2$, are important to produce OH only at high energies (4 eV) when the total rate for electron impact ionization of O_2 and H_2O is high enough. The same is valid for the process $O_2^+ \cdot H_2O + H_2O \rightarrow O_2 + OH + H_3O^+$, which is, beside $NO_3 + H \rightarrow NO_2 + OH$ and $NO_3 + HO_2 \rightarrow O_2 + NO_2 + OH$, included in the pattern part of bars in Figure 4a). When the water vapor is included as a feed gas component (5,000 ppm), the chemical kinetics of OH radical is determined with the same processes (Figure 4b) but percents of contribution in the total OH production

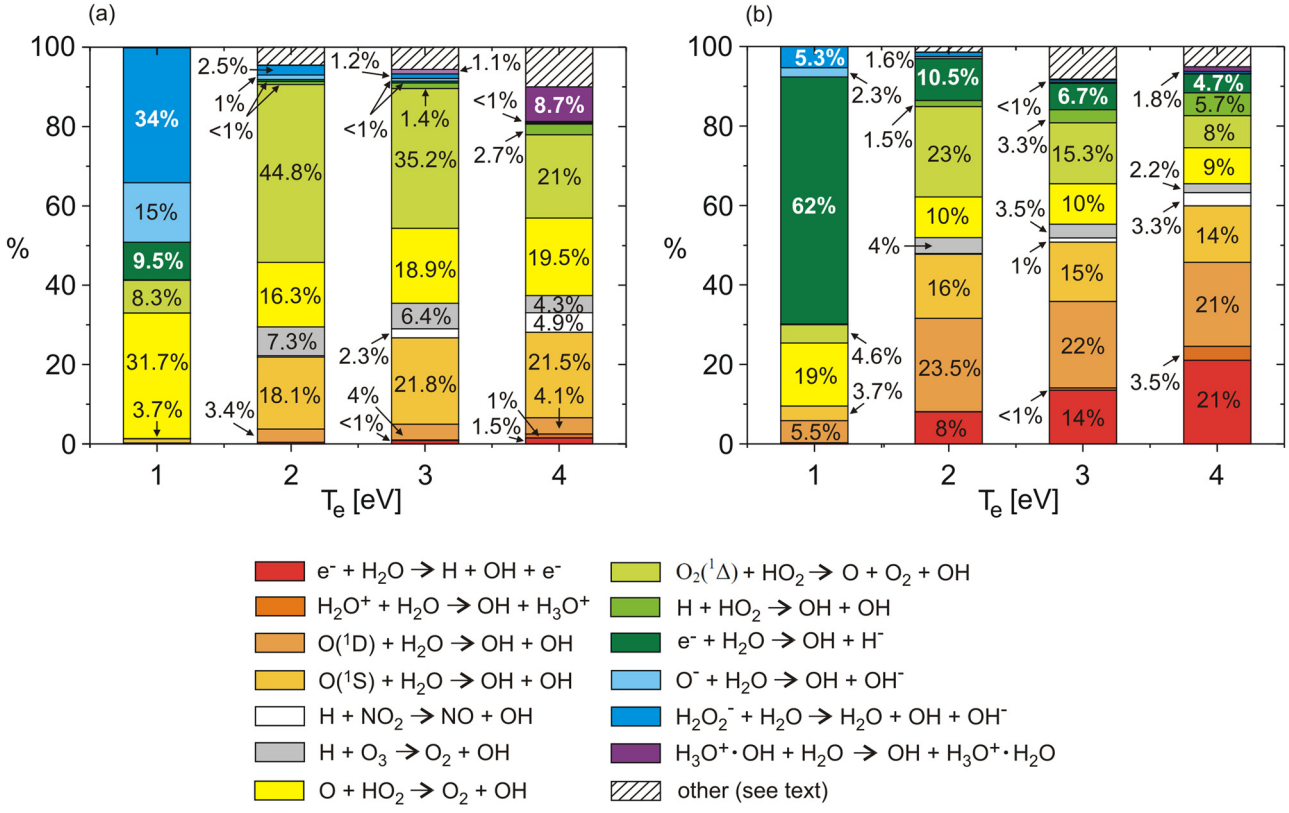

Figure 4: The main production processes of OH radical as a function of mean electron energy for 10,000 ppm of air with 100 ppm H_2O (a) and 5,000 ppm of H_2O (b). Electron concentration is kept constant $n_e = 10^{10}$ cm^{-3} during calculation for 15 ms.

differ than at 100 ppm of H_2O for a several important reasons, apart from different plasma composition. As the first, rate coefficients for electron impact dissociation producing OH, O, O(^{1}D), and O(^{1}S) are influenced by H_2O concentration through modification of EEDF energy tail, as indicated in Figure 1. These effects are even more enhanced in the case of processes with a higher energy threshold such as the ionization of H_2O and O_2, producing ions and hydrates. Second, the influence of water vapor on EEDF and rate coefficients is more pronounced at lower mean electron energies (Figures 1 and 2). As a consequence, dissociative electron attachment to H_2O molecules has the dominant role in the production of OH at 1 eV with more than 60% of contribution and remains important even at higher energies when processes involving excited states O(^{1}D), O(^{1}S), and $O_2(^1\Delta)$ produce OH. Electron impact dissociation of H_2O becomes important above 2 eV, and dominant over the dissociative attachment at 3 and 4 eV. In our model, processes that are included in the pattern part of bars at these energies involve negative ion hydrates: $H_2O^+ + OH^- \cdot H_2O + He \rightarrow H_2O + OH + H_2O + He$ and $O_2^+ \cdot H_2O + OH^- \cdot H_2O + He \rightarrow 2H_2O + He + O_2 + OH$. This also indicates the importance of dissociative attachment to H_2O for the production of OH since these hydrates are mainly produced in the convolution of processes, first $H_2O + e^- \rightarrow H^- + OH$, second $H^- + H_2O \rightarrow OH^- + H_2$, and third $OH^- + H_2O + He \rightarrow OH^- \cdot H_2O + He$, with the total rate proportional to the third power of water vapor concentration in plasma. Finally, according to results presented in Figure 3, concentration of OH at 10,000 ppm of air almost reaches saturation above 3 eV in the interval 10^{13}–10^{14} cm^{-3}, depending on the water vapor mole fraction, due to the increased rate of electron impact dissociation of N_2 molecules and process that convert OH radical into nitric oxide $OH + N \rightarrow NO + H$. Concentration of this reactive species is presented in Figure 5, for $n_e = 10^{10}$ cm^{-3} after 15 ms of calculation.

In our model, nitric oxide is taken as a component of ambient air (10^{-6}%) [17]. For the low amount of air effluent in plasma (dashed lines with scatter symbols), the concentration of NO profoundly rises with the mean electron energy, and it is more influenced by water vapor, as presented in Figure 5, than for 10,000 ppm of air (solid lines with scatter), when similar saturation occurs like in the OH case due to the conversion process $OH + N \rightarrow NO + H$, which couples kinetics of OH and NO. For the purpose of biomedical applications, it is important to reinforce the production of NO, and the discharges with higher amounts of air are used [54]. Having this fact in mind, we have chosen to analyze the main production pathways for NO at 10,000 ppm of air, as presented in Figure 6.

At low amount of water vapor (Figure 6a) and low energies around 1 eV, electron impact dissociation of N_2

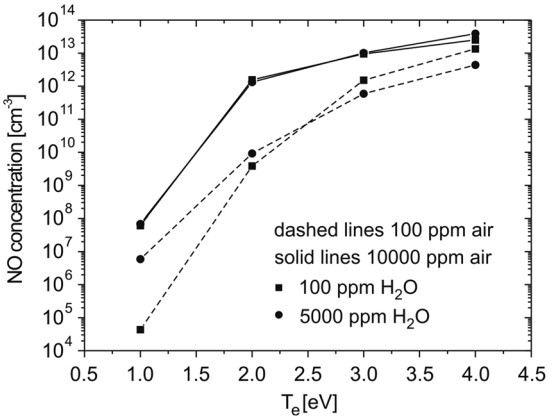

Figure 5: Concentration of NO in plasma as a function of mean electron energy for different amounts of air and water vapor in helium plasma and $n_e = 10^{10}$ cm^{-3}.

(9.7 eV) and conversion process $OH + N \rightarrow NO + H$ do not play an important role in the production of NO, which is then initially generated mainly through the effluent of air in plasma. After 15 ms of global model calculation, the composition of plasma becomes more complex, and we recognize new important generation pathways, which include oxygen atoms $O + NO_2 \rightarrow NO + O_2$ and $O + NO_3^- \rightarrow NO + O_3^-$. The first is a part of a loop of processes since NO generates NO_2 through two-body and three-body association with O, and the second implicates the importance of electron attachment at low energies since NO_3^- ions are mainly generated through charge transfer $O^- + NO_3 \rightarrow NO_3^- + O$ and three-body ion conversion $O^- + NO_2 + He \rightarrow NO_3^- + He$. Beside chemical complicity, these processes become important for creation of NO also because the rate coefficient for dissociation of O_2 (4.5 eV) is a few orders of magnitude higher at 1 eV than for dissociation of N_2, as presented in Figure 2c–d. For mean electron energies of 2 eV or higher, dissociation of H_2O (7.6 eV) takes place in kinetics of NO through processes $OH + N \rightarrow NO + H$ and dissociation of O_2 through channel $O + NO_2 \rightarrow NO + O_2$. At 4 eV, dissociation of N_2 is reinforced enough so that chemical reactions of excited species N(^{2}D) and N(^{2}P) with O_2 molecules also occur as important NO production channels.

If water vapor is included as a feed gas component, the most important pathway for the generation of NO is conversion $OH + N \rightarrow NO + H$ for 2 eV and higher energies, as presented in Figure 6b. Only at 1 eV, this process is competitive with the flow of NO from ambient air. Processes that are included in the pattern part of bars in Figure 6 are $O_2 + N(^2D) \rightarrow O + NO$, $O_2 + N(^2P) \rightarrow O(^1D) + NO$, $O_2 + N(^2P) \rightarrow O(^1S) + NO$, and $N + NO_3 \rightarrow NO + NO_2$, with a few percent of contribution in generation of NO for each, and are excluded from Figure 6 for the purpose of simplicity of presentation.

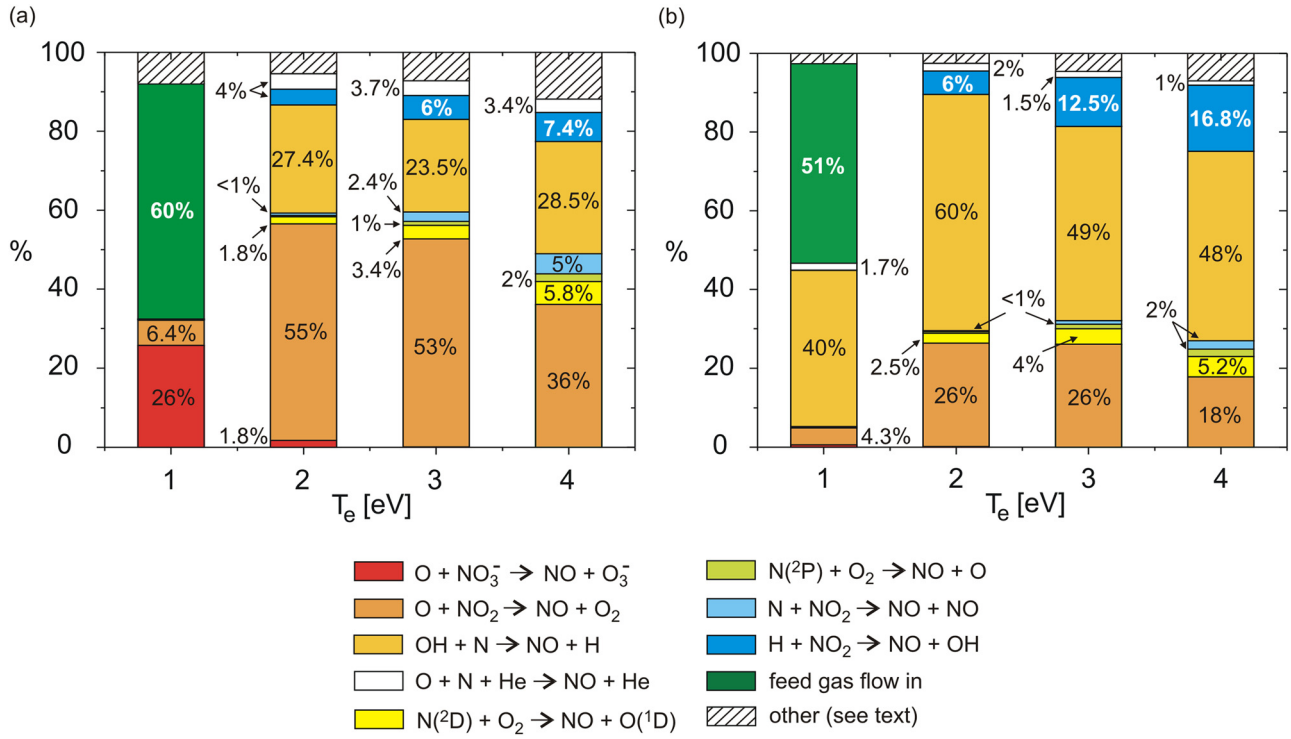

Figure 6: The main production processes of NO as a function of the mean electron energy for 10,000 ppm of air with 100 ppm H_2O (a) and 5,000 ppm of H_2O (b). Electron concentration is kept constant $n_e = 10^{10}$ cm^{-3} during calculation for 15 ms.

3.2 Effect of electron concentration on production of OH and NO

In Figure 7, we present the calculated EEDFs for 1% of air in helium plasma and for a different amount of water vapor and electron concentration. These values are taken as optimal from experimental data in the literature [24], based on LIF measurements for free plasma jet in open air and measurement of electron concentration and temperature for plasma bullets, which propagates in the plasma channel of the jet [14–16,55]. Distributions are also compared with the Maxwell–Boltzmann distribution for the same mean electron energy 1 eV (Figures 7a) and 4 eV (Figure 7b). For electrons behind the ionization front, Maxwellianization effects of EEDF are observable only at electron concentration 10^{14} cm^{-3}, while for 10^{10} cm^{-3} and even 10^{12} cm^{-3}, high energy tail of nonequilibrium EEDF differs from MB tail for a few orders of magnitude. In the case of higher mean electron energies (Figure 7b), water vapor has a negligible influence on EEDF, and the effect of Maxwellianization is not observable even at electron concentration 10^{14} cm^{-3}, which is measured as the highest in cold atmospheric pressure pulsed discharges [16]. As a consequence, rate coefficients for electron impact dissociation of O_2, N_2, and H_2O and other inelastic processes are increased by electron concentration at lower mean electron energies, but not influenced above 3 eV neither by electron concentration nor by water vapor. Similar results are presented in our previous work [42] for a micro-jet with a much lower and constant concentration of air and H_2O. In this work, we present the results of a more complex study for a wide range of discharge conditions based on experimental data presented in the literature.

As it is presented in our previous work [42], the results of a system of coupled particle balance equations in 0D global model calculation are mostly dependent on the variation of rate coefficients with the mean electron energy (electron temperature), reflecting the influence of EEDF. Since the electron temperature has the specific space distributions in plasma bullets and depends on specific plasma discharge, according to the results presented in Figure 7, it can be expected that Maxwellianization effects on EEDF can introduce important differences in the production of OH radical and nitric oxide NO.

With rate coefficients obtained by BOLSIG+ for each set of conditions (water vapor and electron concentration), we have calculated plasma composition after 15 ms and made the analysis of all important chemical pathways for producing OH radical and NO. In Figures 8 and 9, we present the concentration of these reactive species for three different electron concentrations, 10^{10}, 10^{12}, and 10^{14} cm^{-3},

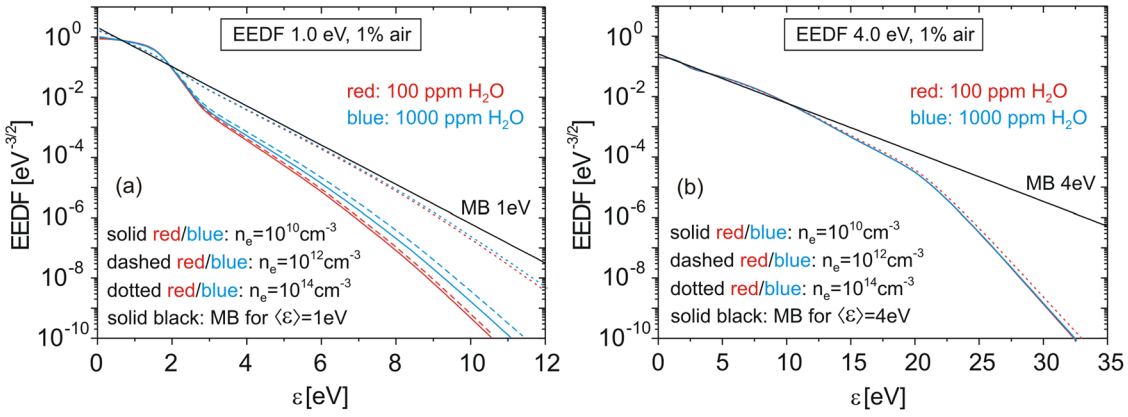

Figure 7: EEDF calculated by BOLSIG + for 1% of air and (a) mean electron energy 1 eV and (b) 4 eV, with 100 ppm (blue lines) and 1,000 ppm H_2O (red lines) and for electron concentration 10^{10} cm^{-3} (solid lines), 10^{12} cm^{-3} (dashed lines), and 10^{14} cm^{-3} (dotted lines). Solid black lines represent Maxwell–Boltzmann EEDF. (b) Calculated EEDFs overlap for a wide range of varied amounts of H_2O and n_e.

and two different amounts of water vapor, 100 ppm and 1,000 ppm, which represent the order of magnitude when water vapor comes only from humidity of ambient air or it is included as feed gas component. Figures also present estimated interval for measured concentrations of OH and NO from the literature [25–27].

To verify our model, we have made the comparison of our calculated results for OH and NO concentration with experimental data from the literature, for the range of electron temperature 1–4 eV and electron concentration 10^{10}–10^{14} cm^{-3} in Figures 8 and 9. Model reaches the good agreement with measured values of OH concentration with those presented by Yonemory *et al.* [24] at all electron temperatures for electron concentration below 10^{12} cm^{-3}, which was also reported by Yonemory *et al.* [24]. Concerning NO, above 1 eV, we reach good agreement with the experimental data in previous studies [25–27] for electron concentration above 10^{12} cm^{-3}, characteristic of pulsed discharges.

As presented in Figure 8, the calculated OH concentration rises with the electron temperature for all values of electron concentrations. At 1 eV, an increase in electron concentration from 10^{10} to 10^{14} cm^{-3} leads to an increase in OH concentration from around 5×10^{11} to 3×10^{14} cm^{-3} (for 100 ppm H_2O) or 1×10^{12} to 5×10^{14} cm^{-3} (for 1,000 ppm H_2O). At high energies (4 eV), an increase in electron concentration increases OH concentration from around 3×10^{13} to 3×10^{15} cm^{-3} (for 100 ppm H_2O) or 5×10^{13} to near 1×10^{16} cm^{-3} (for 1,000 ppm H_2O). These effects of n_e and T_e resemble the Maxwellianization effects on EEDF through the values of rate coefficients and thus total rates of OH production pathways as presented in Figure 4.

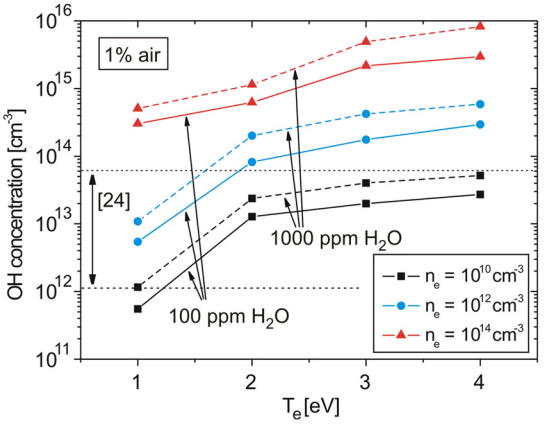

Figure 8: Calculated OH concentration for 1% air in plasma and different concentrations of electrons and water vapor amounts. The estimated interval of measured OH concentration from the literature [24] is also marked.

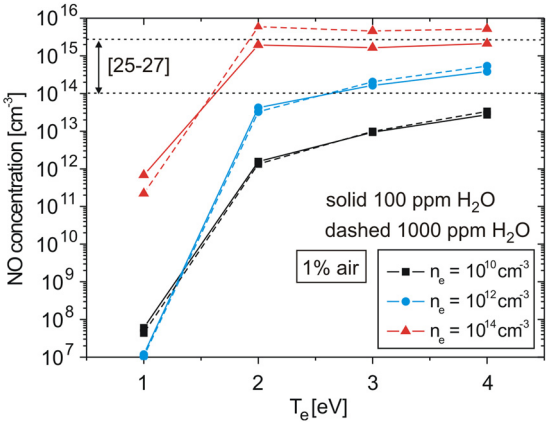

Figure 9: Calculated NO concentration for 1% of air in plasma and different concentrations of electrons and water vapor amounts. The estimated interval of measured NO concentration from the literature [25–27] is also marked.

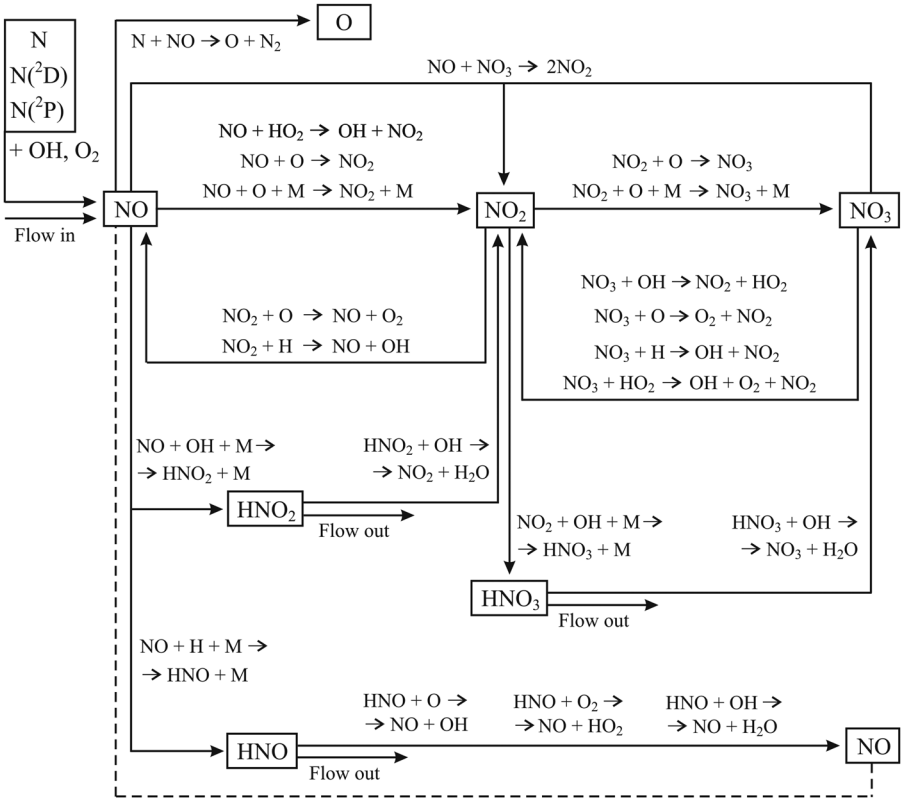

Figure 10: The main production and consumption mechanisms for species NO_x and HNO_x, determined by a 0D global model after 15 ms of calculation.

Having in mind that for biomedical applications the temperature of active medium should be near to body temperature, plasmas with lower mean electron energy are preferable. According to Eq. (2), it is hard to obtain the low electron temperature at high E/N obtained by high absorbed power. According to the results presented in Figure 8, the best agreement between our model results and experimental data is obtained for lower electron temperatures 1–2 eV and electron concentration of 10^{10}–10^{12} cm^{-3}, also reported in the literature as a characteristic for many types of CAPS. So, one can conclude that dissociative attachment to H_2O molecules is very important to produce OH radicals in plasmas at lower mean electron energies.

In both cases, electron concentration and water vapor increase the concentrations of OH and NO, but the best agreement between global model results and measured data is obtained for electron concentration 10^{10} and temperature 2 eV for OH (Figure 8), and some higher values 10^{12} cm^{-3} and 3 eV for NO (Figure 9), due to higher threshold for electron impact dissociation of N_2. These values are also in good agreement with measured electron concentration and temperature for free jet, which propagates in open air from the literature [14–16]. We chose to make an analysis of all important chemical pathways for the production of OH and NO at given conditions.

In the case of OH important production channels for 100 ppm H_2O, $n_e = 10^{10}$ cm^{-3} and $T_e = 2$ eV are presented in Figure 4a), while at 1,000 ppm H_2O, the most important processes are $O(^1D) + H_2O \rightarrow OH + OH$ (15.3%), $O(^1S) + H_2O \rightarrow OH + OH$ (22.2%), $O + HO_2 \rightarrow O_2 + OH$ (13.3%), and $O_2(^1D) + HO_2 \rightarrow O + O_2 + OH$ (32.3%). Dissociative electron attachment and dissociation of H_2O molecules contribute to OH production summary with only 6%.

In the case of NO, at 3 eV and electron concentration 10^{12} cm^{-3}, the most important production channels are $O + NO_2 \rightarrow O_2 + NO$ (22%/11.7%), $N + OH \rightarrow NO + H$ (22.2%/29.4%), and $NO_2 + H \rightarrow NO + OH$ (33%/49%) (percents of contribution are related to 100 and 1,000 ppm of H_2O, respectively).

At the same mean energy but higher electron concentration 10^{14} cm^{-3}, concentration of NO reaches the order of magnitude 10^{15} cm^{-3} (Figure 9), and these processes contribute to total NO production with $O + NO_2 \rightarrow O_2 + NO$ (18%/14%), $N + OH \rightarrow NO + H$ (7%/7.4%), and $NO_2 + H \rightarrow NO + OH$ (46%/48%) at 100 ppm and 1,000 ppm of H_2O, respectively. Moreover, new processes including excited species are recognized as important for the production of NO: $O(^1D) + NO_2 \rightarrow O_2 + NO$ (11.9%/7.7%), and $O(^1D) + N_2O \rightarrow NO + NO$

(3.5%/8.5%), since the main $O(^1D)$ production channel is the electron impact dissociation $e^- + O_2 \rightarrow O + O(^1D) + e^-$ with the total rate profoundly increased with electron concentration and also due to Maxwellianization of EEDF. One should have in mind that these processes occur as important after 15 ms of calculation and are the part of a complex chemical loop, while the initial production of NO is mainly carried by OH conversion with N and flow in from ambient air.

We have made the analysis of all important production and consumption processes for reactive species NO_x and HNO_x for a wide range of discharge conditions, which are presented schematically in Figure 10. The percent of contribution for each process depends on the chemical composition of plasma/humid air mixture and also electron temperature and concentration. As presented, nitric oxide initially comes from flow of air in the plasma and conversion of OH with nitrogen atoms, produced by electron impact dissociation of N_2, and then becomes an important precursor for other reactive nitrogen-oxygen compounds. After a few milliseconds of calculation, chemical composition of the plasma becomes more complex and new chemical pathways, and NO_x becomes important for not only the production of NO but also for the enhanced production of acids HNO_x through three-body association with H and OH, which are then carried out from the system through flow. An analogous scheme representing the chemical kinetics of OH radical with all important pathways is presented in in our paper [17].

4 Conclusion

In this work, we have presented numerical analysis based on the 0D global model, of important production pathways for OH radical and nitric oxide NO for the case of atmospheric pressure low-temperature helium plasma jets, which propagate in open air. The model is based on reaction scheme that comprises 1,488 reactions among 74 species [17]. During calculation, a parametric study was performed with the variation of electron temperature and electron concentration at different amounts of air and water vapor in plasma, with the goal to examine the influence of these important parameters on EEDF and chemical kinetics of OH and NO as precursors for production oxygen and nitrogen reactive species. We have identified the main processes for the production of OH, NO, and NO_x species, for the wide range of conditions based on experimental data given in the literature. Rate coefficients for all electron impact processes included in the model are calculated using the two-term Boltzmann solver BOLSIG+, with cross-sectional data taken mostly from Quantemol-DB and LXCat databases. On the basis of the swarm analysis obtained by BOLSIG+ for the constant electron concentration of $10^{10}\,cm^{-3}$, we found analogously as in our previous work that higher amount of air and water vapor require higher values of reduced electric field to achieve the same mean electron energy, which rises the energy tail of EEDF and consequently more or less increases the values of rate coefficients for electron impact processes, depending on the mean electron energy of EEDF and energy threshold. More important, in this work, we have found that Maxwellization effects of EEDF for lower mean energies are observable only at electron concentration $10^{14}\,cm^{-3}$, while for $10^{10}\,cm^{-3}$ and even $10^{12}\,cm^{-3}$, high energy tail of nonequilibrium EEDF differ from MB tail for a few orders of magnitude. In the case of higher mean energies, the effect of Maxwellization is not observable even at electron concentration $10^{14}\,cm^{-3}$, which is presented in the literature as the highest measured value in cold atmospheric pressure pulsed discharges.

In this work, we have also shown that dissociative attachment has the important role in the production of OH. When water vapor comes only from the humidity of ambient air, the main role in the OH production takes attachment to O_2 through process $O^- + H_2O \rightarrow OH + OH^-$ and the pathway that include $H_2O_2^-$ ions produced in analogous 3-body association with He as a third body. Also, at higher mean energies, we found that important pathways are reactions of species $O(^1D)$ and $O(^1S)$ with H_2O and also process involving hydrate $H_3O^+ \cdot OH$, produced in $O_2^+ \cdot H_2O + H_2O \rightarrow H_3O^+ \cdot OH + O_2$ and process involving hydrate $H_3O^+ \cdot OH$, produced in $O_2^+ \cdot H_2O + H_2O \rightarrow H_3O^+ \cdot OH + O_2$. If water vapor is included as a feed gas component, dissociative attachment to H_2O molecules has the dominant role in the production of OH with more than 60% of contribution at lower mean electron energies (for electrons behind the ionization front), with observable contribution even at higher energies when processes involving excited states $O(^1D)$, $O(^1S)$, and $O_2(^1\Delta)$ produce OH. Electron impact dissociation of H_2O becomes important above 2 eV, and more pronounced than dissociative attachment at 3 and 4 eV. In our model at higher mean energies, we recognize the processes that involve negative ion hydrates, $H_2O^+ + OH^- \cdot H_2O + He \rightarrow H_2O + OH + \cdot H_2O + He$ and $O_2^+ H_2O + OH^- H_2O + He \rightarrow 2H_2O + He + O_2 + OH$. This result also indicates the importance of dissociative attachment to H_2O for the production of OH, since these hydrates are mainly produced in the convolution of processes, the first $H_2O + e^- \rightarrow H^- + OH$, the second $H^- + H_2O \rightarrow OH^- + H_2$, and the third $OH^- + H_2O + He \rightarrow OH^- \cdot H_2O + He$.

Concerning NO, results of our model show that the conversion process $OH + N \rightarrow NO + H$ does not play an important role in the production of this species at low

mean electron energies when water vapor comes only from the humidity of ambient air, due to low amount of H_2O in plasma but also to the low rate of electron impact dissociation of N_2. For these conditions, NO is initially generated mainly through the effluent of air in plasma. We recognize new important generation pathways which include oxygen atoms $O + NO_2 \rightarrow NO + O_2$ and $O + NO_3^- \rightarrow NO + O_3^-$. The second implicates again the importance of electron dissociative attachment at low energies since NO_3^- ions, according to the results of our model, are mainly generated through charge transfer $O^- + NO_3 \rightarrow NO_3^- + O$ and three body ion conversion $O^- + NO_2 + He \rightarrow NO_3^- + He$. For higher mean energies above 2 eV, dissociation of H_2O takes place in the production of NO through $OH + N \rightarrow NO + H$ and dissociation of O_2 through production channel $O + NO_2 \rightarrow NO + O_2$. At 4 eV, dissociation of N_2 is reinforced enough so that excited species $N(^2D)$ and $N(^2P)$ reacting with O_2 molecules take a role in the production of NO. If water vapor is included as a feed gas component, the most important pathway for generation of NO is conversion of $OH + N \rightarrow NO + H$ for a wide range of conditions, while only at 1 eV, this process is a competitive with the flow of NO from ambient air. Finally, we have schematically presented all important processes recognized by our model, which determine the chemical kinetics of NO_x and HNO_x species for a wide range of varied conditions, concerning electron temperature, concentration, and amount of air and water vapor in a plasma.

Funding information: This work was supported by MPNTR of Serbia. We thank the Ministry of Science, Technological Development, and Innovation of the Republic of Serbia for support under Contract No. 451-03-65/2024-03/200124.

Author contributions: All authors have accepted responsibility for the entire content of this manuscript and approved its submission.

Conflict of interest: The authors state no conflict of interest.

Data availability statement: The datasets generated and/or analyzed during the current study are available from the corresponding author on reasonable request.

References

[1] von Woedtke T, Laroussi M, Gherardi M. Foundations of plasmas for medical applications. Plasma Sources Sci Technol. 2022;31:054002.

[2] Bruggeman PJ, Iza F, Brandenburg R. Foundations of atmospheric pressure non-equilibrium plasmas. Plasma Sources Sci Technol. 2017;26:123002.

[3] Levchenko I, Xu S, Mazouffre S, Lev D, Pedrini D, Goebel D, et al. Perspectives, frontiers, and new horizons for plasma-based space electric propulsion. Phys Plasmas. 2020;27:020601.

[4] Foster JE, Garcia MC. Promise of nonthermal plasmas in addressing emerging environmental and health problems: Present and future. Phys Plasmas. 2022;29:060601.

[5] Adamovich I, Baalrud S, Bogaerts A, Bruggeman PJ, Cappelli M, Colombo V, et al. The 2017 Plasma Roadmap: Low temperature plasma science and technology. J Phys D: Appl Phys. 2017;50:323001.

[6] Kong MG, Kroesen G, Morfill G, Nosenko T, Shimizu T, Van Dijk J, et al. Plasma medicine: an introductory review. N J Phys. 2009;11:115012.

[7] Weltmann KD, von Woedtke T. Plasma medicine—current state of research and medical application. Plasma Phys Control Fusion. 2017;59:014031.

[8] Graves DB. The emerging role of reactive oxygen and nitrogen species in redox biology and some implications for plasma applications to medicine and biology. J Phys D: Appl Phys. 2012;45:263001.

[9] Metelmann HR, Nedrelow DS, Seebauer C, Schuster M, von Woedtke T, Weltmann KD, et al. Head and neck cancer treatment and physical plasma. Clin Plasma Med. 2015;3:17–23.

[10] Gorbanev Y, Maldonado AP, Bogaerts A. Analysis of short-lived reactive species in plasma–air–water systems: The dos and the do nots. Anal Chem. 2018;90:22.

[11] Sun B, Liu D, Wang X, Liu Z, Iya F, Yang A, et al. Reactive species in cold atmospheric-pressure He + Air plasmas: The influence of humidity. Phys Plasmas. 2019;26:063514.

[12] Van Gaens W, Bogaerts A. Kinetic modelling for an atmospheric pressure argon plasma jet in humid air. J Phys D: Appl Phys. 2014;46:079502.

[13] Ghimire B, Sornsakdanuphap J, Hong YJ, Uhm HS, Weltmann KD, Choi EH. The effect of the gap distance between an atmospheric-pressure plasma jet nozzle and liquid surface on OH and N2 species concentrations. Phys Plasmas. 2017;24:073502.

[14] Chang Z, Zhang G, Shao X, Zhang Z. Diagnosis of gas temperature, electron temperature, and electron density in helium atmospheric pressure plasma jet. Phys Plasmas. 2012;19:073513.

[15] Lin L, Lyu Y, Trink B, Canady J, Keidar M. Cold atmospheric helium plasma jet in humid air environment. J Appl Phys. 2019;125:153301.

[16] Nikiforov AY, Leys C, Gonzalez MA, Walsh JL. Electron density measurement in atmospheric pressure plasma jets: Stark broadening of hydrogenated and non-hydrogenated lines. Plasma Sources Sci Technol. 2015;24:034001.

[17] Mladenović Ž, Gocić S. Influence of air and water vapor on EEDF, plasma parameters, and the main RONS in atmospheric pressure low temperature helium plasmas: Global model approach. Phys Plasmas. 2022;29:103504.

[18] Schröter S, Wijaikhum A, Gibson AR, West A, Davies HL, Minesi N, et al. Chemical kinetics in an atmospheric pressure helium plasma containing humidity. Phys Chem Chem Phys. 2018;20:24263–86.

[19] Naidis GV. Modelling of plasma bullet propagation along a helium jet in ambient air. J Phys D: Appl Phys. 2011;44:215203.

[20] Lu X, Laroussi M, Puech V. On atmospheric-pressure non-equilibrium plasma jets and plasma bullets. Plasma Sources Sci Technol. 2012;21:034005.

[21] Liu XY, Pei XK, Ostrikov K, Lu XP, Liu DW. The production mechanisms of OH radicals in a pulsed direct current plasma jet. Phys Plasmas. 2014;21:093513.

[22] Liu Z, Wang W, Liu D, Zhou C, He T, Xia W, et al. Experimental investigation of behavior of bullets dynamics and production of RONS in helium APPJs-liquid interaction: The effect of additive gas components. Phys Plasmas. 2019;26:053507.
[23] Liu Y, Tan Z, Chen X, Li X, Zhang H, Pan J, et al. An investigation on the effects of air on electron energy in atmospheric pressure helium plasma jets. Phys Plasmas. 2018;25:033514.
[24] Yonemory S, Nakagawa Y, Ono R, Oda T. Measurement of OH density and air–helium mixture ratio in an atmospheric-pressure helium plasma jet. J Phys D: Appl Phys. 2012;45:225202.
[25] Yonemory S, Ono R. Effect of discharge polarity on the propagation of atmospheric-pressure helium plasma jets and the densities of OH, NO, and O radicals. Biointerphases. 2015;10:029514.
[26] van Gessel AFH, Alards KMJ, Bruggeman PJ. NO production in an RF plasma jet at atmospheric pressure. J Phys D: Appl Phys. 2013;46:265202.
[27] Ono R. Optical diagnostics of reactive species in atmospheric-pressure nonthermal plasma. J Phys D: Appl Phys. 2016;49:083001.
[28] Brisset A, Gibson AR, Schröter S, Niemi K, Booth J-P, Gans T, et al. Chemical kinetics and density measurements of OH in an atmospheric pressure He + O2 + H2O radiofrequency plasma. J Phys D: Appl Phys. 2021;54:285201.
[29] Hurlbatt A, Gibson AR, Schröter S, Bredin J, Foote APS, Grondein P, et al. Concepts, capabilities, and limitations of global models: A review. Plasma Process Polym. 2017;14:1600138.
[30] Liu Y, Liu D, Zhang J, Sun B, Yang A, Kong MG. 1D fluid model of RF-excited cold atmospheric plasmas in helium with air gas impurities. Phys Plasmas. 2020;27:043512.
[31] Liu DX, Rong MZ, Wang XH, Iza F, Kong MG, Bruggeman P. Main species and physicochemical processes in cold atmospheric-pressure He + O_2 plasmas. Plasma Process Polym. 2010;7:846.
[32] Bruggeman P, Schram DC. On OH production in water containing atmospheric pressure plasmas. Plasma Sources Sci Technol. 2010;19:045025.
[33] Liu DX, Bruggeman P, Iza F, Rong MZ, Kong MG. Global model of low-temperature atmospheric-pressure He + H_2O plasmas. Plasma Sources Sci Technol. 2010;19:025018.
[34] Norberg SA, Johnsen E, Kushner MJ. Formation of reactive oxygen and nitrogen species by repetitive negatively pulsed helium atmospheric pressure plasma jets propagating into humid air. Plasma Sources Sci Technol. 2015;24:035026.
[35] Stalder KR, Vidmar RJ, Nersisyan G, Graham WG. Modeling the chemical kinetics of high-pressure glow discharges in mixtures of helium with real air. J Appl Phys. 2006;99:093301.
[36] Liu DX, Iza F, Wang XH, Kong MG, Rong MZ. He + O_2 + H_2O plasmas as a source of reactive oxygen species. Appl Phys Lett. 2011;98:221501.
[37] Sakiyama Y, Graves DB, Chang HW, Shimizu T, Morfill GE. Plasma chemistry model of surface microdischarge in humid air and dynamics of reactive neutral species. J Phys D:Appl Phys. 2012;45:425201.
[38] Murakami T, Niemi K, Gans T, O'Connell D, Graham WG. Chemical kinetics and reactive species in atmospheric pressure helium–oxygen plasmas with humid-air impurities. Plasma Sources Sci Technol. 2013;22:015003.
[39] Sun B, Liu D, Wang X, Liu Z, Iza F, Yang A, et al. Reactive species in cold atmospheric-pressure He + Air plasmas: The influence of humidity. Phys Plasmas. 2019;26:063514.
[40] Sun B, Liu D, Yang A, Rong M, Wang X. Global model of cold atmospheric He + air plasmas: A comparison of Maxwellian and non-Maxwellian EEDFs. Phys Plasmas. 2019;26:123508.
[41] Jiang Y, Wang Y, Zhang J. Numerical study on the production and transport of O and OH in a helium–humid air atmospheric pressure plasma jet interacting with a substrate. Phys Plasmas. 2021;28:103501.
[42] Mladenović Ž, Gocić S, Marić D, Petrović ZL. Influence of space charge density on electron energy distribution function and on composition of atmospheric pressure He/O_2/air plasmas. Eur Phys J Plus. 2018;133:344.
[43] Murakami T, Niemi K, Gans T, O'Connell D, Graham DG. Interacting kinetics of neutral and ionic species in an atmospheric-pressure helium–oxygen plasma with humid air impurities. Plasma Sources Sci Technol. 2013;22:045010.
[44] Gocić S, Mladenović Ž. Global model simulation of OH production in pulsed-DC atmospheric pressure helium-air plasma jets. Open Phys. 2018;16:375–82.
[45] Bruggeman PJ, Kushner MJ, Locke BR, Gardeniers JGE, Graham WG, Graves DB, et al. Plasma–liquid interactions: a review and roadmap. Plasma Sources Sci Technol. 2016;25:053002.
[46] Sun B, Liu D, Iza F, Wang S, Yang A, Liu Z, et al. Global model of an atmospheric-pressure capacitive discharge in helium with air impurities from 100 to 10 000 ppm. Plasma Sources Sci Technol. 2019;28:035006.
[47] Hagelaar GJM, Pitchford LC. Solving the Boltzmann equation to obtain electron transport coefficients and rate coefficients for fluid models. Plasma Sources Sci Technol. 2005;14:722–33.
[48] Morgan database. www.lxcat.net. Retrieved on April 24, 2019.
[49] Tennyson J, Rahimi S, Hill C, Tse L, Vibhakar A, Akello-Egwel D, et al. QDB: A new database of plasma chemistries and reactions. Plasma Sources Sci Technol. 2017;26:055014.
[50] Elsaid EM, Wahid TZA, Morad AM. Exact solutions of plasma flow on a rigid oscillating plate under the effect of an external non-uniform electric field. Results Phys. 2020;19:103554.
[51] Viegas P, Slikboer E, Bonaventura Z, Guaitella O, Sobota A, Bourdon A. Physics of plasma jets and interaction with surfaces: review on modelling and experiments. Plasma Sources Sci Technol. 2022;31:053001.
[52] Balcon N, Hagelaar G, Boeuf J. Numerical model of an argon atmospheric pressure RF discharge. IEEE Trans Plasma Sci. 2008;36:2782–7.
[53] Schröter S, Gibson AR, Kushner MJ, O'Connell D. Numerical study of the influence of surface reaction probabilities on reactive species in an rf atmospheric pressure plasma containing humidity. Plasma Phys Control Fusion. 2018;60:014035.
[54] van Gessel AFH, Hrycak B, Jasiński M, Mizeraczyk J, van der Mullen JJAM, Bruggeman PJ. Temperature and NO density measurements by LIF and OES on an atmospheric pressure plasma jet. J Phys D: Appl Phys. 2013;46:095201.
[55] Schmidt-Bleker A, Winter J, Bösel A, Reuter S, Weltmann K-D. On the plasma chemistry of a cold atmospheric argon plasma jet with shielding gas device. Plasma Sources Sci Technol 2016;25:015005.